

1 INTRODUCTION

2 Above Earth's atmosphere are the Van Allen radiation belts, a toroidally-shaped  
3 pair of belts that consist of a complex and dynamic plasma environment. The inner  
4 radiation belt consists of mostly energetic protons, is very stable on year time scales,  
5 and is located within 2 Earth radii (measured near the equator) above Earth's Earth's  
6 surface. The outer radiation belt, on the other hand, consists of mostly energetic  
7 electrons, is highly dynamic on day, and even hour time scales, and is typically  
8 found between 4 and 8 Earth radii above Earth's surface. The radiation belts pose a  
9 challenge to space exploration due to their effects on our technology-driven society.  
10 Some of the effects include: a higher radiation dose for astronauts and cosmonauts,  
11 degradation of silicon to the point where transistors malfunction, computer memory  
12 corrupts due to bit flips, etc. With these effects in mind, it is no surprise that the  
13 radiation belts have been extensively studied since their discovery in the 1960s.

14 The radiation belt plasma is at times unstable which in turn generate electric and  
15 magnetic waves. These waves in turn accelerate and scatter radiation belt particles  
16 with a variety of wave-particle mechanisms. One form of wave-particle interactions  
17 scatter particles into Earth's atmosphere in the form of electron microbursts.

18 Electron microbursts, henceforth referred to as microbursts, are typically  
19 observed by low Earth orbiting spacecraft, sounding rockets, and high altitude  
20 balloons as a sub-second impulse of electrons. Some of the most intense microbursts  
21 have electron fluxes that are a factor of 10 to 100 above the background (for example  
22 see Fig. 7 in Blake et al. (1996)). Since they were first reported by Anderson and  
23 Milton (1964), the intense transient nature of microbursts have compelled countless  
24 researchers to understand their properties, their effects on the environment, and the  
25 physical mechanism(s) that create microbursts. Microbursts are widely believed

26 to be created by wave-particle scattering between a plasma wave called whistler  
 27 mode chorus and outer radiation belt electrons, although many details regarding the  
 28 scattering mechanism are unconstrained or unknown. The goal of this dissertation is  
 29 to study the wave-particle scattering mechanism that scatters electron microbursts.

30 This chapter serves as an introduction to the fundamental physical concepts  
 31 that are essential to understand wave-particle interactions in Earth's magnetosphere.  
 32 We will first derive the motion of individual charged particles in Earth's electric and  
 33 magnetic fields. Next we will cover how various groups of charged particles coalesce  
 34 to form the major particle populations in the magnetosphere. Then, we will cover  
 35 the various mechanisms that accelerate and scatter particles in the magnetosphere.  
 36 Lastly, we will review microbursts, which is one of the loss mechanism, as a jumping-  
 37 off point for the rest of the dissertation.

38 Charged Particle Motion in Electric and Magnetic Fields

A charged particle trapped in the magnetosphere will experience three types of periodic motion in Earth's nearly dipolar magnetic field. The three motions are ultimately due to the Lorentz force that a particle of momentum  $\vec{p}$ , charge  $q$ , and velocity  $\vec{v}$  experiences in an electric field  $\vec{E}$  and magnetic field  $\vec{B}$  and is given by

$$\frac{d\vec{p}}{dt} = q(\vec{E} + \vec{v} \times \vec{B}). \quad (1.1)$$

39 In the magnetosphere, the three periodic motions, in decreasing frequency, are  
 40 gyration, bounce, and drift and are schematically shown in Fig. 1.1. Each periodic  
 41 motion has a corresponding conserved quantity i.e. an adiabatic invariant.

The highest frequency periodic motion is gyration about a magnetic field of

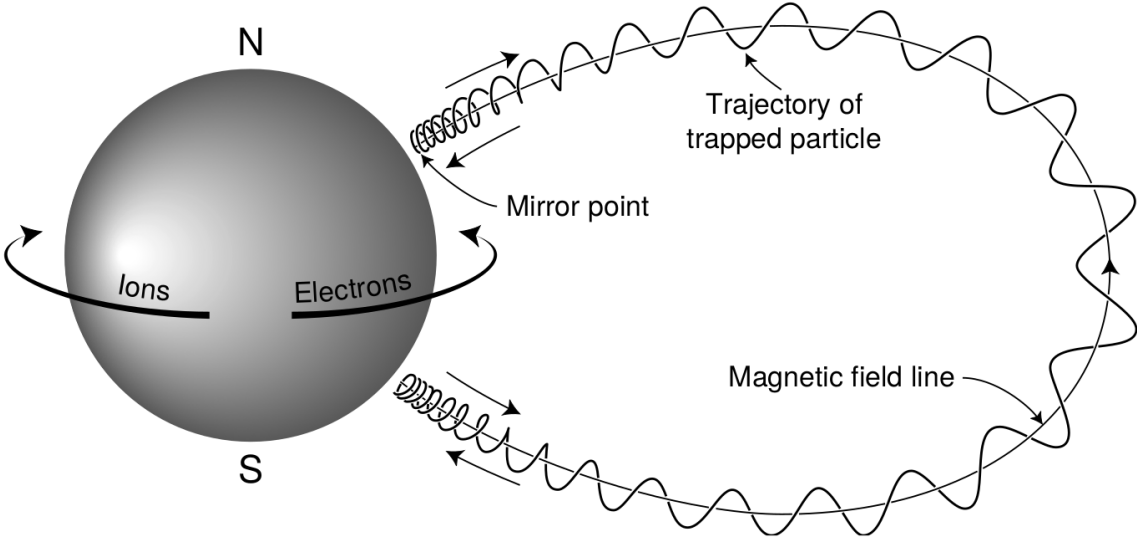


Figure 1.1: The three periodic motions of charged particles in Earth's dipole magnetic field. These motions are: gyration about the magnetic field line, bounce motion between the magnetic poles, and azimuthal drift around the Earth. Figure from (Baumjohann and Treumann, 1997).

magnitude  $B$ . This motion is circular with a Larmor radius of

$$r = \frac{mv_{\perp}}{|q|B} \quad (1.2)$$

where  $m$  is the mass and  $v_{\perp}$  the particle's velocity perpendicular to  $\vec{B}$ . This motion has a corresponding gyrofrequency

$$\Omega = \frac{|q|B}{m} \quad (1.3)$$

in units of radians/second. In the radiation belts, the electron gyrofrequency,  $\Omega_e$  is on the order of a kHz. The corresponding adiabatic invariant is found by integrating the particle's canonical momentum around the particle's path of gyration

$$J_i = \oint (\vec{p} + q\vec{A}) \cdot d\vec{l} \quad (1.4)$$

42 where  $J_i$  is the  $i^{th}$  adiabatic invariant and  $\vec{A}$  is the magnetic vector potential. This  
 43 integral is carried out by integrating the first term over the circumference of the  
 44 gyro orbit and integrating the second term using Stokes theorem to calculate the  
 45 magnetic flux enclosed by the gyro orbit. The gyration invariant is  $J_1 \sim v_{\perp}^2/B$ , which  
 46 is conserved when the frequency,  $\omega$  of a force acting on the gyrating electron satisfies  
 47  $\omega \ll \Omega_e$ .

48 The second highest frequency periodic motion is bouncing due to a parallel  
 49 gradient in  $\vec{B}$ . This periodic motion naturally arises in the magnetosphere because  
 50 Earth's magnetic field is stronger near the poles, and artificially in the laboratory  
 51 in magnetic bottle machines. To understand this motion we first we need to define  
 52 the concept of pitch angle,  $\alpha$  as the angle between  $\vec{B}$  and  $\vec{v}$  which is schematically  
 53 shown in Fig. 1.2a. The pitch angle relates  $v$  with  $v_{\perp}$ , and  $v_{\parallel}$  (the component of the  
 54 particles velocity parallel to  $\vec{B}$ ). As shown in Fig. 1.2b and 1.2c, a smaller (larger)  
 55  $\alpha$  will increase (decrease) the distance that the charged particle travels parallel to  $\vec{B}$ ,  
 56 during one gyration.

Assuming the particle's kinetic energy is conserved, the conservation of  $J_1$   
 implies that given a particle's  $v_{\perp}(0)$  and  $B(0)$  at the magnetic equator (where  
 Earth's magnetic field is usually at a minimum), we can calculate its  $v_{\perp}(s)$  along the  
 particle's path  $s$  by calculating  $B(s)$  from magnetic field models. Thus the particle's  
 perpendicular velocity is then related via

$$\frac{v_{\perp}^2(0)}{B(0)} = \frac{v_{\perp}^2(s)}{B(s)} \quad (1.5)$$

57 which can be rewritten as

$$\frac{v^2 \sin^2 \alpha(0)}{B(0)} = \frac{v^2 - v_{\parallel}^2(s)}{B(s)} \quad (1.6)$$

<sup>58</sup> and re-arranged to solve for  $v_{||}(s)$

$$v_{||}(s) = v \sqrt{1 - \frac{B(s)}{B(0)} \sin^2 \alpha(0)} \quad (1.7)$$

<sup>59</sup> which will tend towards 0 when the second term in the radical approaches 1.

<sup>60</sup> The location where  $v_{||}(s) = 0$  is called the mirror point and is where a particle  
<sup>61</sup> reverses direction. Since Earth's magnetic field is stronger towards the poles, the  
<sup>62</sup> mirroring particle will execute periodic bounce motion between its two mirror points  
<sup>63</sup> in the northern and southern hemispheres. The corresponding adiabatic invariant,  $J_2$   
<sup>64</sup> is

$$J_2 = \oint p_{||} ds \quad (1.8)$$

where  $ds$  describes the particle path between the mirror points in the northern and southern hemispheres (see Fig. 1.1).  $J_2$  is found by substituting Eq. 1.7 into Eq. 1.8 and defining the magnetic field strength at the mirror points as  $B_m$  (where  $\alpha(m) = 90^\circ$ ). The  $J_2$  integral can be written as

$$J_2 = 2p \int_{m_n}^{m_s} \sqrt{1 - \frac{B(s)}{B(m)}} ds \quad (1.9)$$

<sup>65</sup> where  $m_n$  and  $m_s$  are the northern and southern mirror points, respectively. The  
<sup>66</sup> bounce period can be estimated (e.g. Baumjohann and Treumann, 1997) to be

$$t_b \approx \frac{LR_e}{\sqrt{W/m}} (3.7 - 1.6 \sin \alpha(0)) \quad (1.10)$$

<sup>67</sup> where  $W$  is the particle's kinetic energy, and  $L$  is the  $L$ -shell.  $L$ -shell describes the  
<sup>68</sup> distance from the Earth's center to the location where a particular magnetic field  
<sup>69</sup> line crosses the magnetic equator, in units of Earth radii,  $R_e$ . As with gyration, the

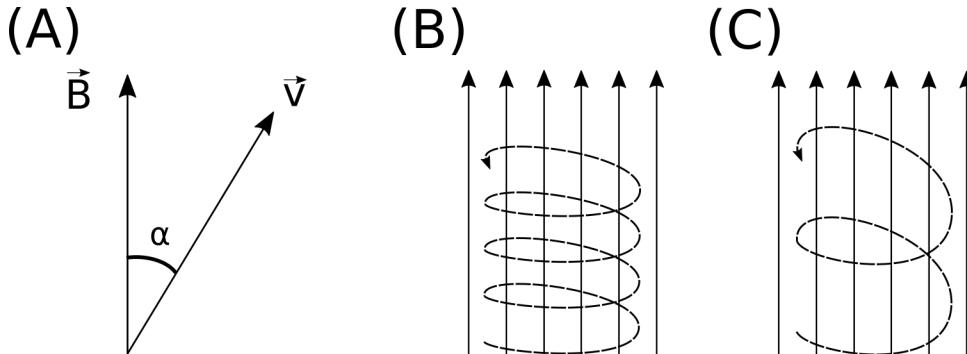


Figure 1.2: Charged particle motion in a uniform magnetic field  $\vec{B}$ . Panel (A) shows the geometry defining the pitch angle,  $\alpha$ . Panel (B) and (C) show two helical electron trajectories with dashed lines assuming a large and small  $\alpha$  (corresponding to a small and large parallel velocity  $v_{||}$ ), respectively.

70 particle will bounce between the mirror points as long as  $\omega \ll \Omega_b$ , where  $\Omega_b$  is the  
71 bounce frequency.

72 At this stage it is instructional to introduce the notion of the loss cone pitch  
73 angle,  $\alpha_L$ . A particle with  $\alpha \leq \alpha_L$  will mirror at or below  $\approx 100$  km altitude in  
74 the atmosphere. A charged particle gyrating at those altitudes will encounter and  
75 Coulomb scatter with the dense atmosphere and be lost from the magnetosphere.

76 The slowest periodic motion experienced by charged particles in Earth's mag-  
77 netic field is azimuthal drift around the Earth. This drift results from a combination of  
78 a radial gradient in  $\vec{B}$  and the curvature of the magnetic field. The radial gradient drift  
79 arises because Earth's magnetic field is stronger near the Earth where the particle's  
80 gyroradius radius of curvature shrinks as it gyrates towards stronger magnetic field,  
81 and expands when it gyrates outward. The overall effect is the particle gyro orbit does  
82 not close on itself and negatively charged particles drift east and positively charged  
83 particles drift west. The radial gradient drift is further enhanced by the centrifugal  
84 force that a particle experiences as it bounces along the curved field lines. The drift  
85 adiabatic invariant,  $J_3$  is found by integrating Eq. 1.4 over the complete particle orbit

86 around the Earth. The shape of this drift orbit is known as a drift shell. For  $J_3$ , the  
 87 first term is negligible and the second term is the magnetic flux enclosed by the drift  
 88 shell,  $\Phi_m$  i.e.  $J_3 \sim \Phi_m$ .

89 Figure 1.3 from Schulz and Lanzerotti (1974) shows contours of the gyration,  
 90 bounce, and drift frequencies for electrons and protons in Earth's dipole magnetic  
 91 field.

Up until now we have considered the three periodic motions due Earth's magnetic field in the absence of electric fields. If there is an electric field,  $E_\perp$  perpendicular to  $\vec{B}$ , a particle's center of gyration i.e., averaged position of the particle over a gyration, will drift with a velocity perpendicular to both  $E_\perp$  and  $\vec{B}$ . The drift velocity can be solved using Eq. 1.1 and is

$$\vec{v}_E = \frac{\vec{E} \times \vec{B}}{B^2}. \quad (1.11)$$

92 If there is a parallel magnetic field,  $E_{||}$  then the particle is accelerated along the  
 93 magnetic field line. An  $E_{||}$  pointing away from the Earth will contribute to the mirror  
 94 force and raise the particle's mirror point. On the contrary, an Earthward pointing  
 95  $E_{||}$  will oppose the mirror force and lower the mirror point. If the Earthward  $E_{||}$  is  
 96 strong enough, the mirror point is lowered into the atmosphere that will precipitate  
 97 particles. This is the mechanism that generates the aurora.

98 Particle Populations and Their Interractions in the Magnetosphere

99 Now that we have looked at the dynamics of single-particle motion in electric  
 100 and magnetic fields, we will briefly tour the various macroscopic populations in the  
 101 magnetosphere that are illustrated in Fig. 1.4.

102 The sun and its solar wind are ultimately the source of energy input into the  
 103 magnetosphere. The solar wind at Earth's orbit is a plasma traveling at supersonic

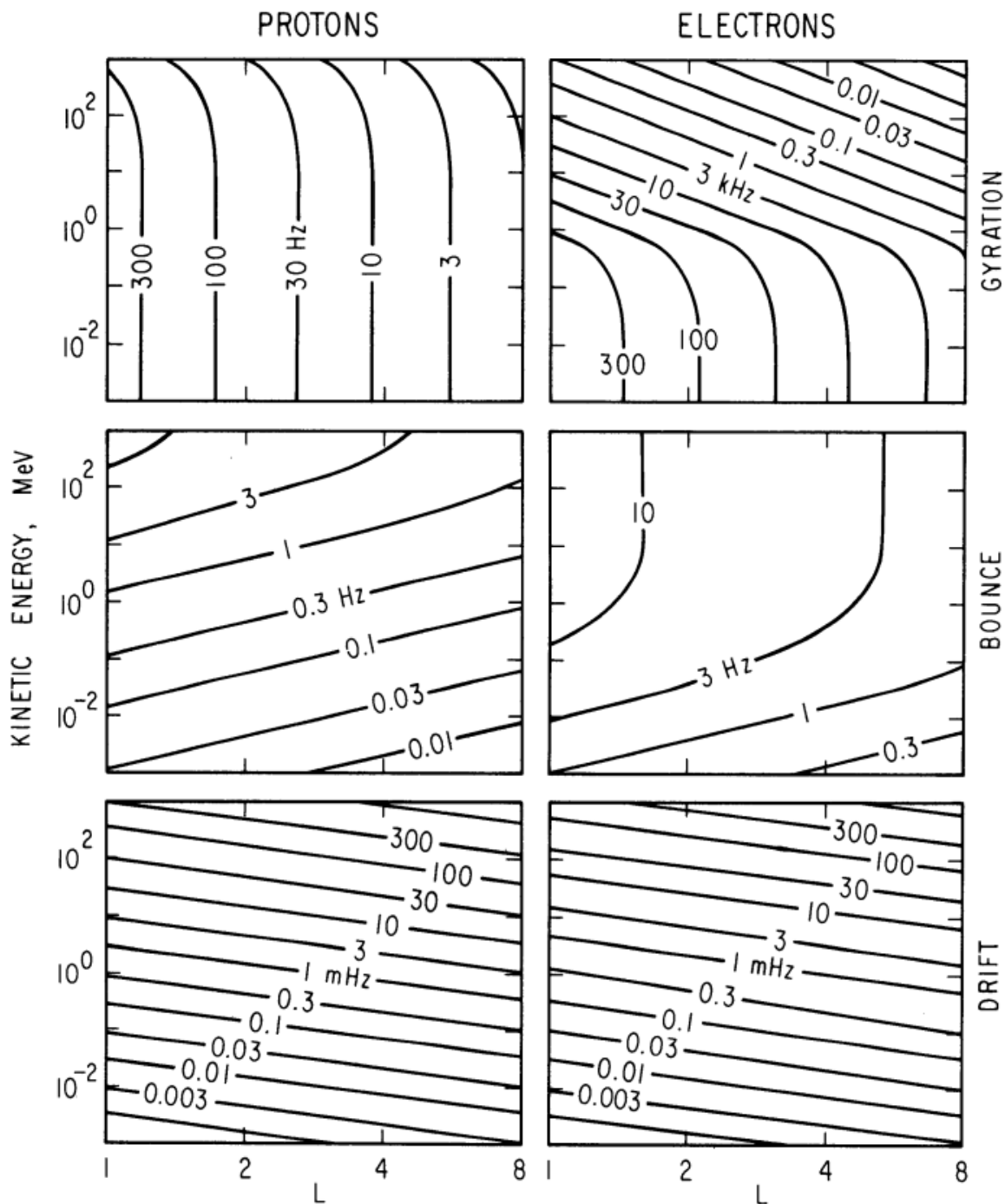


Figure 1.3: Contours of constant gyration, bounce, and drift frequencies for electrons and protons in a dipole field. Figure from Schulz and Lanzerotti (1974).

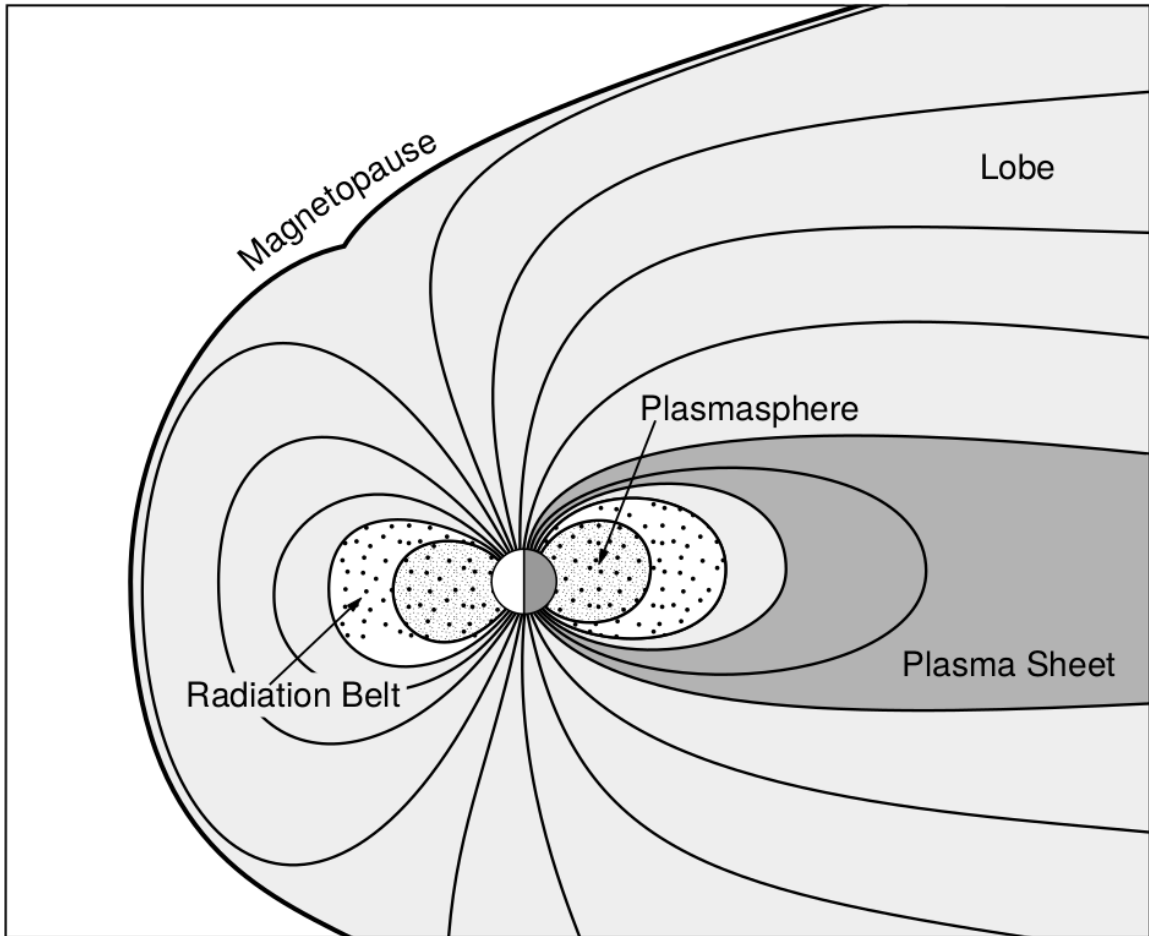


Figure 1.4: A few macroscopic structures in the magnetosphere. The magnetosphere boundary with the solar wind is the magnetopause. The magnetotail consists of two lobes that contain Earth's magnetic flux with the plasma sheet separating the two lobes. The inner magnetosphere contains the plasmasphere, the ring current, and the radiation belts which are co-located. Figure from Baumjohann and Treumann (1997).

speeds with an embedded interplanetary magnetic field (IMF). When the solar wind encounters Earth's magnetic field, the plasma can not easily penetrate into the magnetosphere because the plasma is frozen-in on magnetic field lines. Thus the plasma and its magnetic field drapes around the magnetosphere, forming a cavity in the solar wind that qualitatively has a shape as shown in Fig. 1.4. Because the solar wind is supersonic at 1 AU, a bow shock exists upstream of the magnetosphere. The solar wind plasma, after it is shocked by the bow shock, flows around the magnetosphere inside the magnetosheath. The surface where the solar wind ram pressure and Earth's magnetic pressure balance is termed the magnetopause, which can be thought of as a boundary between the solar wind and Earth's magnetosphere. This is a slightly naive description of the magnetopause, but is nonetheless an instructive conceptual picture. The shocked plasma then flows past the Earth where it shapes the magnetotail. In the magnetotail the magnetopause exists where the solar wind magnetic pressure balances Earth's magnetic field pressure in the lobes. The magnetotail extends on the order of  $100 R_E$  downstream of Earth, and the tailward stretching of magnetic field lines creates the plasma sheet which exists in the region of low magnetic field strength near the magnetic equator (e.g. Eastwood et al., 2015).

## 121 Populations in the Inner Magnetosphere

Closer to Earth, where the magnetic field is largely dipolar, are three plasma populations that comprise the inner magnetosphere: the plasmasphere, the ring current, and the radiation belts which are shown in Fig. 1.4. Before we describe these three particle populations in detail, we will first introduce the coordinate system that most naturally describes the inner magnetosphere environment, and then the electric fields that effect mostly low energy particles.

In this coordinate system the “radial” coordinate was defined in section 1 and

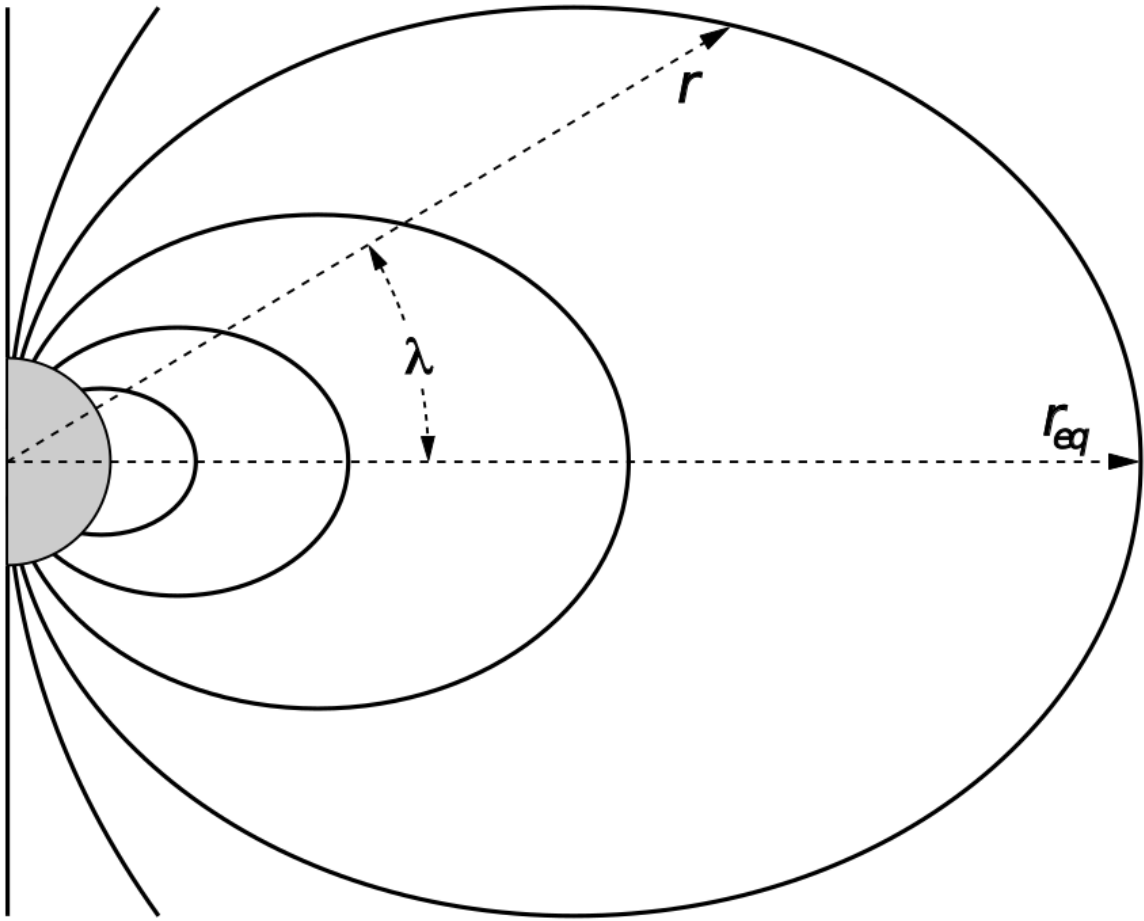


Figure 1.5: The dipole coordinate system. The magnetic latitude of  $\mathbf{r}$  is  $\lambda$ . The radial distance to a magnetic field line in the equatorial plane is typically given by  $L = r_{eq}/R_e$ . Figure from Baumjohann and Treumann (1997).

is the L shell. The azimuthal coordinate is the magnetic local time (MLT). For an observer above Earth's north pole looking down, MLT is defined to be 0 (midnight) in the anti-sunward direction, and increases in the counter-clockwise direction with 6 at dawn, 12 at noon (sunward direction), and 18 in dusk. The final coordinate is the magnetic latitude,  $\lambda$  which is analogous to the latitude coordinate in the spherical coordinate system, and is defined to be 0 at the magnetic equator. This coordinate system is shown in Fig. 1.5 and naturally describes the inner magnetosphere populations described below.

137        The low energy particle dynamics in the inner magnetosphere are organized by  
 138        two electric fields: the co-rotation and the dawn-dusk electric fields. The co-rotation  
 139        electric field arises from Earth's rotation. The magnetic field and the particles frozen  
 140        on it rotate with the Earth. To a non-rotating observer this rotation appears as a  
 141        radial electric field that drops off as  $\sim L^{-2}$ . The other electric field, pointing from  
 142        dawn to dusk is called the convection electric field and is due to the Earthward  
 143        transport of particles from the magnetotail that appears as an electric field in Earth's  
 144        reference frame. The superposition of the co-rotation and convection electric  
 145        fields is a potential field shown in Fig. 1.6. The shaded area in Fig. 1.6 shows the  
 146        orbits on which low energy electrons are trapped, and outside this region the particles  
 147        are not trapped. The dynamic topology of the shaded region in Fig. 1.6 is controlled  
 148        by only the convection electric field which is dependent on the solar wind speed and  
 149        the IMF. The lowest energy particles that orbit in the shaded region in Fig. 1.6 make  
 150        up the plasmasphere.

151        Plasmasphere The plasmasphere is a dense ( $n_e \sim 10^3/\text{cm}^3$ ), cool ( $\sim \text{eV}$ )  
 152        plasma. The plasmasphere typically extends to  $L \sim 4$  and the spatial extent is  
 153        highly dependent on the solar wind and magnetospheric conditions. The source  
 154        of the plasmasphere is the ionosphere. The two main mechanisms that fill the  
 155        plasmasphere with cold plasma are ionization of the ionosphere by sunlight and  
 156        particle precipitation. The ultraviolet ionization by sunlight is strongly dependent  
 157        on the time of day (day vs night), latitude (more ionization near the equator). The  
 158        ionization due to particle precipitation, on the other hand, is highly dependent on  
 159        magnetospheric conditions, and mostly occurs at high latitudes.

160        The outer boundary of the plasmasphere is the plasmapause which is typically  
 161        identified as a steep radial gradient in plasma density from  $\sim 10^3/\text{cm}^3$  to  $\sim 1/\text{cm}^3$ .

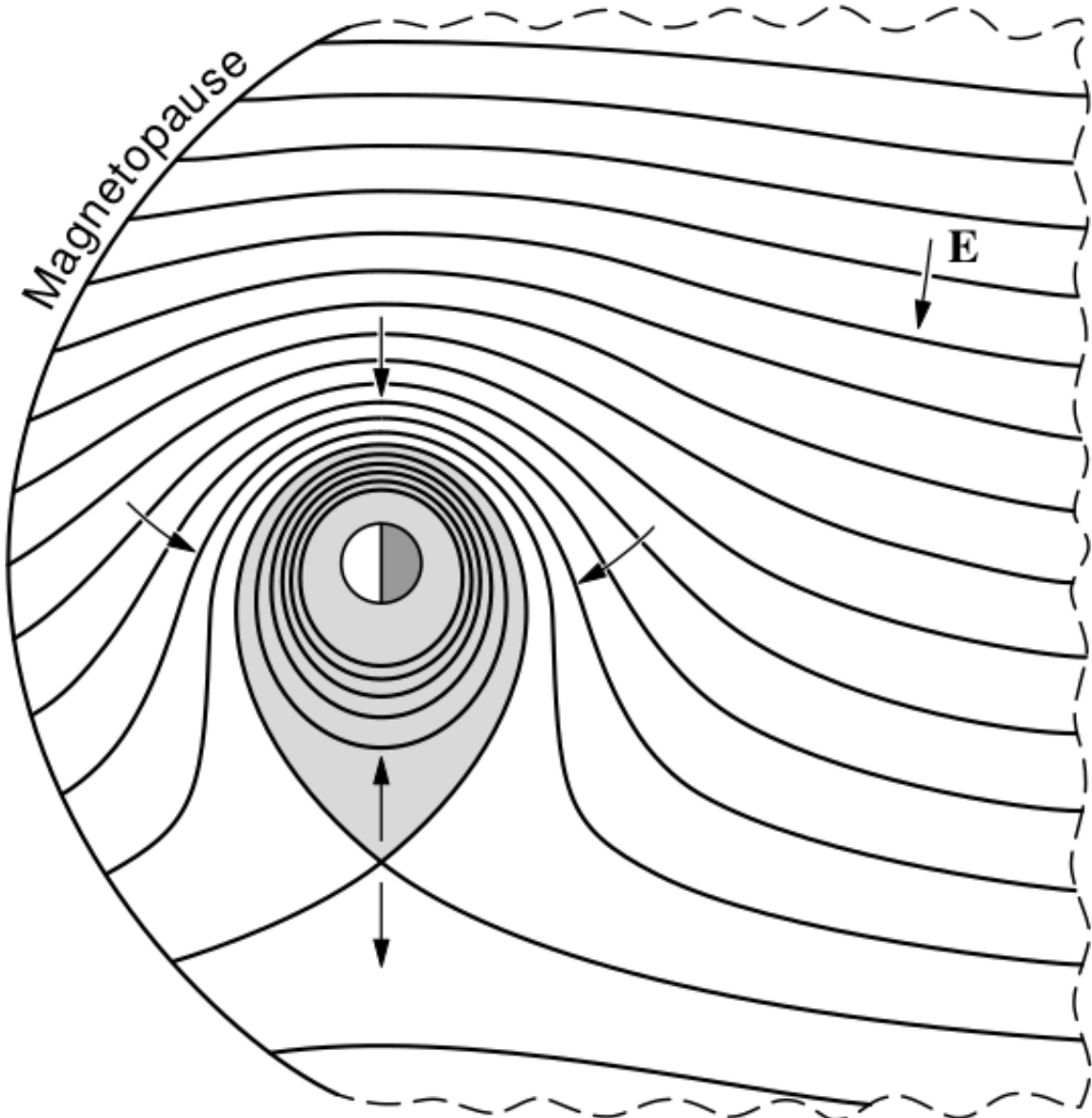


Figure 1.6: Equipotential lines and electric field arrows due to the superposition of the co-rotation and convection electric fields. Electrons in the shaded region execute closed orbits. Outside of the shaded regions the electrons are not trapped and will escape. The region separating the two regimes is called the Alfvén layer. Figure from Baumjohann and Treumann (1997).

<sub>162</sub> The location of the plasmapause is important to model (e.g. O'Brien and Moldwin,  
<sub>163</sub> 2003) and understand since the plasma density strongly controls the efficiency of  
<sub>164</sub> particle scattering by waves (e.g. Horne et al., 2005).

<sub>165</sub>        Ring Current The next higher energy population is the ring current. This  
<sub>166</sub> population consists of protons and electrons between tens and a few hundred keV  
<sub>167</sub> that drift around the Earth. The orbits of higher energy particles are not as effected  
<sub>168</sub> by the convection and co-rotation electric field, rather they drift around the Earth  
<sub>169</sub> due to gradient and curvature drifts. Since the direction of the drift is dependent on  
<sub>170</sub> charge, protons drift west around the Earth and electrons drift East. This has the  
<sub>171</sub> effect of creating a current around the Earth.

<sub>172</sub>        The ring current generates a magnetic field which decreases the magnetic field  
<sub>173</sub> strength at the surface of the Earth and increases it outside of the ring current.  
<sub>174</sub> The decrease of Earth's magnetic field strength is readily observed by a system of  
<sub>175</sub> ground-based magnetometers and is merged into a Disturbance Storm Time (DST)  
<sub>176</sub> index to quantify the global reduction in the magnetic field. An example of a DST  
<sub>177</sub> index time series from the 2015 St. Patrick's Day storm, driven by a coronal mass  
<sub>178</sub> ejection (CME), is shown in Fig. 1.7. A few notable features of the storm and the  
<sub>179</sub> ring current are worth pointing out. At the start of the storm the ring current is  
<sub>180</sub> sometimes depleted and DST increases slightly (termed the initial phase or sudden  
<sub>181</sub> storm commencement). Then the ring current population is rapidly built up and  
<sub>182</sub> DST rapidly decreases during the main phase. Lastly, after the storm passes, the  
<sub>183</sub> ring current gradually decays toward its equilibrium state over a period of a few  
<sub>184</sub> days and DST returns towards 0 during the recovery phase. The DST index (along  
<sub>185</sub> with other geomagnetic indices) are readily used by the space physics community to  
<sub>186</sub> quantify the global state of the magnetosphere.

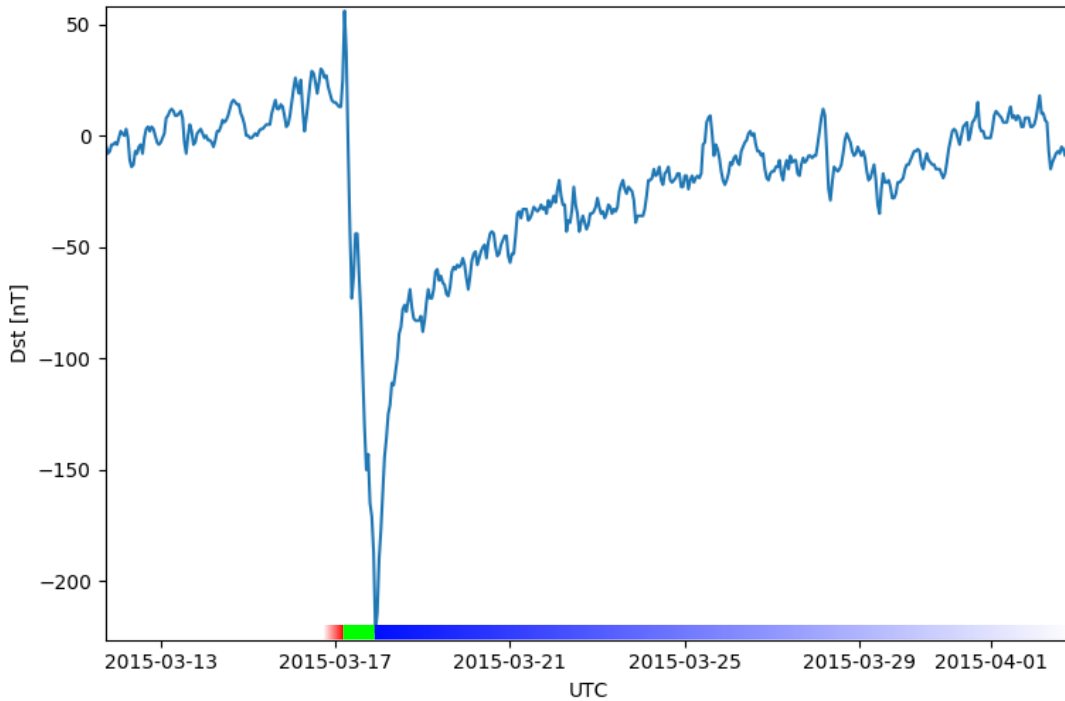


Figure 1.7: The DST index during the St. Patrick's Day 2015 storm. This storm was caused by a coronal mass ejection on March 15th, 2015. The storm phases are: initial phase, main phase, and recovery phase. The initial phase occurred when the Dst peaked at  $+50$  nT on March 17th during which the ring current was eroded by the coronal mass ejection during the interval shown by the red bar shown at the bottom. Then the following rapid decrease to  $\approx -200$  nT was during the main phase where many injections from the magnetotail enhanced the ring current, which reduced Earth's magnetic field strength at the ground, and is shown with the green bar. Lastly, the recovery phase lasted from March 18th to approximately March 29th during which the ring current particles were lost and the ring current returned to its equilibrium state. The recovery phase is shown with the blue bar.

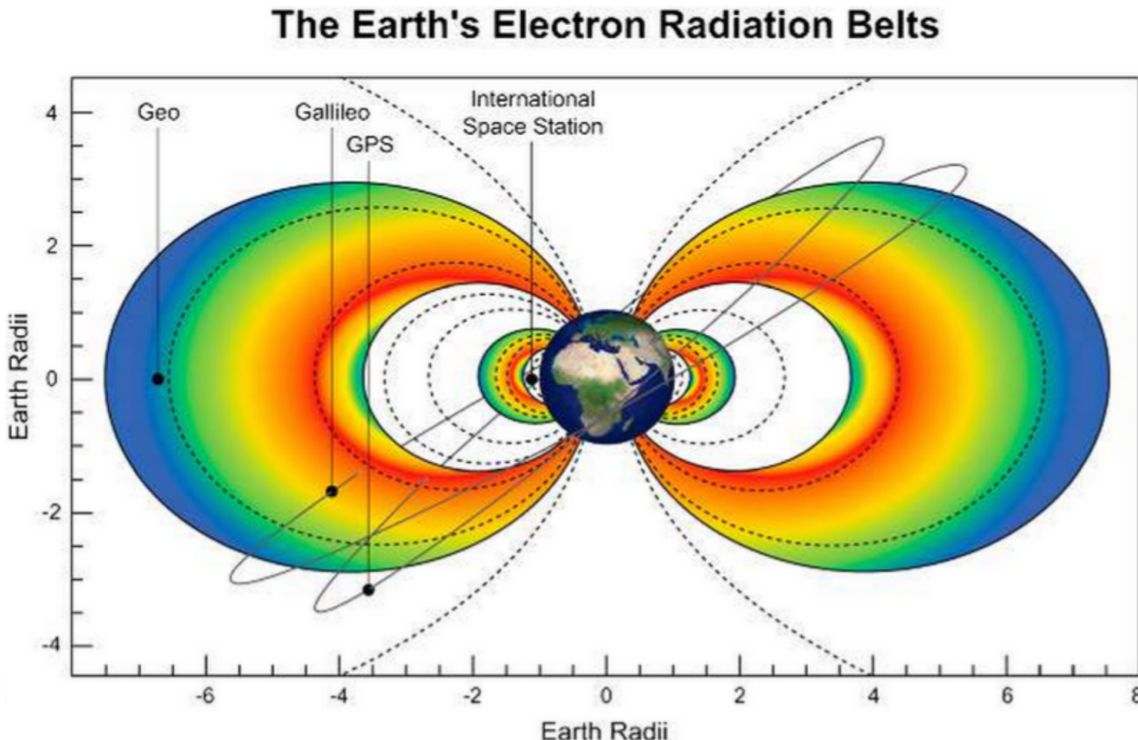


Figure 1.8: The two radiation belts with the locations of various satellites and orbits. Figure from (Horne et al., 2013).

187        Radiation Belts The highest particle energy populations are in the Van Allen  
 188        radiation belts. These belts were discovered by Van Allen (1959) and Vernov and  
 189        Chudakov (1960) during the Cold War and are a pair of toroidally shaped populations  
 190        of trapped electrons and protons shown in Fig. 1.8. Their quiescent toroidal shape,  
 191        similar to the shape of the plasmasphere and ring current, is a result of Earth's dipole  
 192        magnetic field.

193        The inner radiation belt is extremely stable on time periods of years, extends  
 194        to  $L \approx 2$ , and mainly consists of protons with energies between MeV and GeV and  
 195        electrons with energies up to  $\approx 1$  MeV (Claudepierre et al., 2019). The source of  
 196        inner radiation belt protons is believed to be due to cosmic-ray albedo neutron decay  
 197        (e.g. Li et al., 2017) and inward radial diffusion for electrons (e.g. O'Brien et al.,

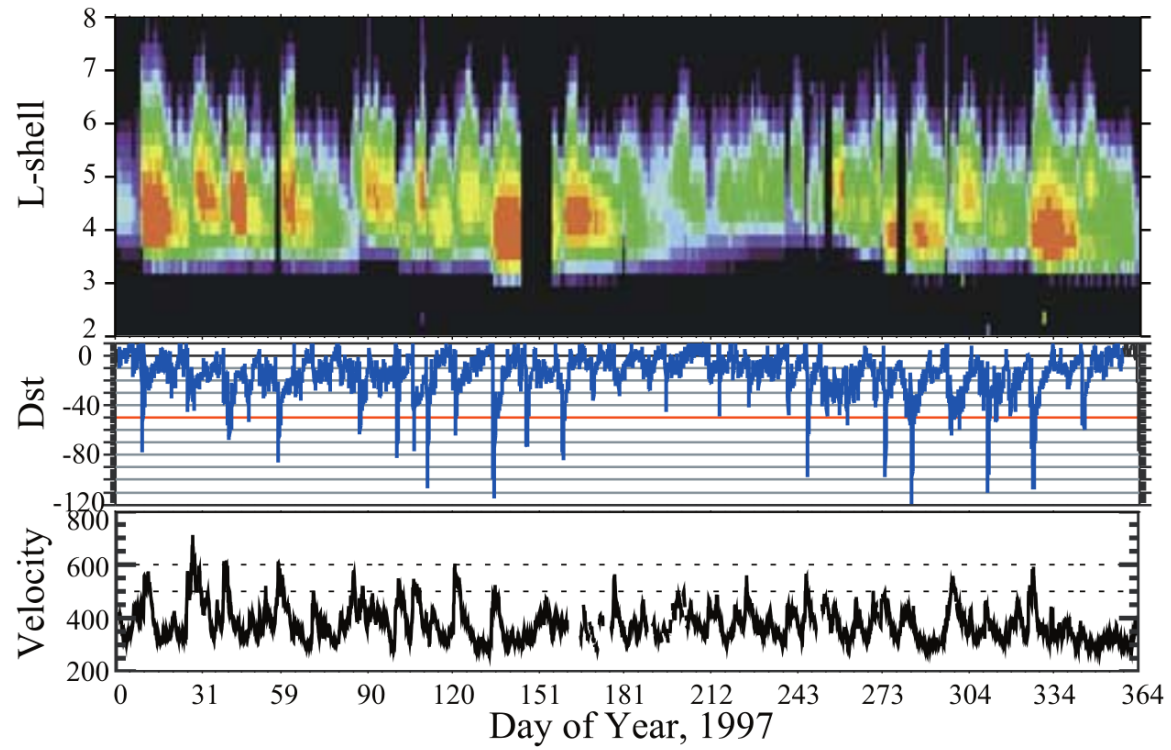


Figure 1.9: The dynamics of the outer radiation belt in 1997 from the POLAR satellite. Top panel shows the 1.2-2.4 MeV electron flux as a function of L and 1997 day of year. The middle panel shows the DST index, and bottom panel shows the solar wind velocity. Figure from (Reeves et al., 2003).

<sup>198</sup> 2016). The gap between the inner and outer radiation belt is called the slot, which is  
<sup>199</sup> believed to be due to hiss waves inside the plasmasphere (described below) scattering  
<sup>200</sup> particles into the atmosphere (e.g. Breneman et al., 2015; Lyons and Thorne, 1973).

<sup>201</sup> The outer radiation belt is much more dynamic and consists of mainly electrons  
<sup>202</sup> of energies up to a few MeV. The outer belt's spatial extent is highly variable as  
<sup>203</sup> shown in Fig. 1.9, and is typically observed between L of 4 and 8. The source of  
<sup>204</sup> outer radiation belt electrons is widely believed to be injections of plasma from the  
<sup>205</sup> magnetotail that is then accelerated to high energies.

<sup>206</sup> Due to the highly energetic and dynamic nature of the radiation belts, and their  
<sup>207</sup> impact on human presence in space, the radiation belts have been studied for over  
<sup>208</sup> half century. Researchers have studied and attempted to predict the dynamics of  
<sup>209</sup> radiation belt particles, waves, and wave-particle interactions by considering various  
<sup>210</sup> competing particle acceleration and loss mechanisms which are described next.

<sup>211</sup> Radiation Belt Particle Sources and Sinks

<sup>212</sup> Adiabatic Heating

<sup>213</sup> One of the particle heating and transport mechanisms arises from the Earthward  
<sup>214</sup> convection of particles. The conservation of  $J_1$  implies that the initial and final  $v_\perp$   
<sup>215</sup> depends on the change in the magnetic field amplitude

$$\frac{v_{\perp i}^2}{B_i} = \frac{v_{\perp f}^2}{B_f}. \quad (1.12)$$

<sup>216</sup> As a particle convects Earthward,  $B_f > B_i$  thus  $v_\perp$  must increase. The dipole  
<sup>217</sup> magnetic field amplitude can be written as

$$B(L, \theta) = \frac{31.2 \mu\text{T}}{L^3} \sqrt{1 + 3 \cos^2 \theta}. \quad (1.13)$$

<sub>218</sub> The change in  $v_{\perp}^2$  can be found by taking the ratio of  $B(L, \theta)$  at two different  $L$  shells

$$\frac{v_{\perp f}^2}{v_{\perp i}^2} = \left( \frac{L_i}{L_f} \right)^3 \quad (1.14)$$

<sub>219</sub> thus the increase in  $v_{\perp} \sim (L_i/L_f)^{3/2}$ .

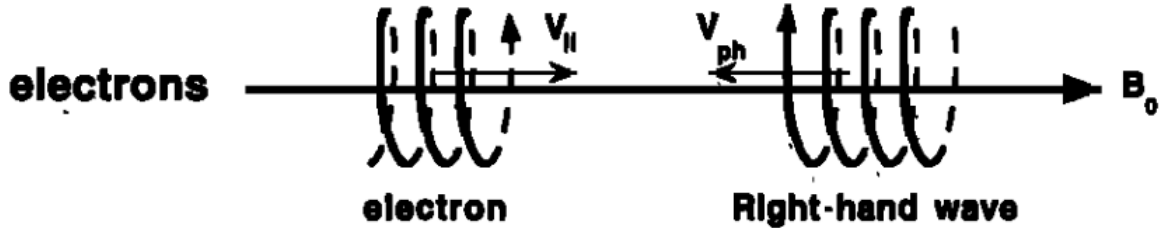
<sub>220</sub> As the particle convects Earthward its  $v_{\parallel}$  also increases because the distance  
<sub>221</sub> between the particle's mirror points decrease. If  $J_2$  is conserved, the shrinking bounce  
<sub>222</sub> path implies that  $v_{\parallel}$  must increase by

$$\frac{v_{\parallel f}^2}{v_{\parallel i}^2} = \left( \frac{L_i}{L_f} \right)^k \quad (1.15)$$

<sub>223</sub> where  $k$  ranges from 2 for equatorial pitch angles,  $\alpha_{eq} = 0^\circ$ , to 2.5 for  $\alpha_{eq} = 90^\circ$   
<sub>224</sub> (Baumjohann and Treumann, 1997). Since the rate of adiabatic heating is greater in  
<sub>225</sub> the perpendicular direction than heating in the parallel direction, an initially isotropic  
<sub>226</sub> particle distribution will become anisotropic during its convection. These isotropic  
<sub>227</sub> particles can then become unstable to wave growth and generate waves in order to  
<sub>228</sub> reach equilibrium.

### <sub>229</sub> Wave Resonance Heating

<sub>230</sub> Another mechanism that heats particles is due to particles resonating with  
<sub>231</sub> plasma waves. A few of the electromagnetic wave modes responsible for particle  
<sub>232</sub> acceleration (and scattering) relevant to radiation belt dynamics are hiss, whistler  
<sub>233</sub> mode chorus (chorus), and electromagnetic ion cyclotron (EMIC) waves. These waves  
<sub>234</sub> are created by the loss cone instability that is driven by an anisotropy of electrons for  
<sub>235</sub> chorus waves, and protons for EMIC waves. The level of anisotropy can be quantified  
<sub>236</sub> by the ratio of the perpendicular to parallel particle temperatures ( $T_{\perp}/T_{\parallel}$ ). A particle  
<sub>237</sub> distribution is unstable when  $T_{\perp}/T_{\parallel} > 1$ . Since electrons gyrate in a right-handed



$$\omega + k_{\parallel} v_{\parallel} = \Omega^-$$

Figure 1.10: The trajectories of an electron and a right-hand circularly polarized wave during a cyclotron resonance. The electron's  $v_{\parallel}$  and the wave's  $k_{\parallel}$  are in opposite directions such that the wave's frequency is Doppler shifted to an integer multiple of the electron cyclotron frequency. Figure from (Tsurutani and Lakhina, 1997).

<sup>238</sup> sense, the chorus waves also tend to be right hand circularly polarized (Tsurutani and  
<sup>239</sup> Lakhina, 1997). The same argument also applies to protons and left hand circularly  
<sup>240</sup> polarized EMIC waves.

<sup>241</sup> These circularly polarized waves can resonate with electrons and/or protons  
<sup>242</sup> when their relative motion results in a static  $\vec{E}$ . One example of a resonance between  
<sup>243</sup> a right hand circularly polarized wave and an electron is shown in Fig. 1.10. The  
<sup>244</sup> electron's  $v_{\parallel}$  and the wave's parallel wave vector,  $k_{\parallel}$  are in opposite directions such  
<sup>245</sup> that the wave frequency  $\omega$  is Doppler shifted to an integer multiple of the  $\Omega_e$  where the  
<sup>246</sup> electron feels a static electric field and is accelerated or decelerated. Quantitatively,  
<sup>247</sup> this resonance condition is easier to understand with the following toy model.

<sup>248</sup> Assume a uniform magnetic field  $\vec{B} = B_0 \hat{z}$  with a parallel propagating ( $k = k \hat{z}$ ),  
<sup>249</sup> right-hand circularly polarized wave. The wave's electric field as a function of position  
<sup>250</sup> and time can be written as

$$\vec{E} = E_0(\cos(\omega t - kz)\hat{x} + \sin(\omega t - kz)\hat{y}). \quad (1.16)$$

The angular component of  $\vec{E}$  that will effect the particle's  $v_{\perp}$  is

$$E_{\theta} = \vec{E} \cdot \hat{\theta} = E_0 \cos(\omega t - kz + \theta). \quad (1.17)$$

<sup>251</sup> Now assume that the electron is traveling in the  $-\hat{z}$  direction with a velocity  $\vec{v} = -v_0 \hat{z}$

<sup>252</sup> so its time dependent position along  $\hat{z}$  is

$$z(t) = -v_0 t \quad (1.18)$$

<sup>253</sup> and gyrophase is

$$\theta(t) = -\Omega t + \theta(0) \quad (1.19)$$

<sup>254</sup> where the first negative sign comes from the electron's negative charge. Now we put  
<sup>255</sup> this all together and find the force that the electron will experience

$$m \frac{dv_{\theta}}{dt} = q E_{\theta} = q E_0 \sin((\omega + kv_0 - \Omega)t + \theta(0)). \quad (1.20)$$

<sup>256</sup> This is a relatively complex expression, but when the time dependent component is  
<sup>257</sup> 0, i.e.

$$\omega + kv_0 - \Omega = 0, \quad (1.21)$$

<sup>258</sup> the electron will feel a static electric field and be accelerated or decelerated depending  
<sup>259</sup> on  $\theta_0$ , the phase between the wave and the electron. The expression in Eq. 1.21 is  
<sup>260</sup> commonly referred to as the resonance condition and is more generally written as

$$\omega - k_{||} v_{||} = \frac{n \Omega_e}{\gamma} \quad (1.22)$$

261 where  $n$  is the resonance order, and  $\gamma$  is the relativistic correction (e.g. Millan and  
 262 Thorne, 2007). In the case of the cyclotron resonance,  $\omega \approx \Omega_e$  thus  $J_1$  is violated.  
 263 Since  $J_1$  is violated,  $J_2$  and  $J_3$  are also violated since the conditions required to violate  
 264  $J_2$  and  $J_3$  are less stringent than  $J_1$ . It is important to remember that a particle will  
 265 experience the effects of many waves along its drift orbit. The typical MLT extent  
 266 of a handful of waves that are capable of resonating with radiation belt electrons are  
 267 shown in Fig. 1.11.

268 Particle Losses

269 Now that we have seen two general mechanisms with which particles are  
 270 accelerated in the magnetosphere, we will now consider a few specific mechanisms  
 271 that remove particles from the magnetosphere into the atmosphere or the solar  
 272 wind. One mechanism that transports magnetosperic particles into the solar wind  
 273 is magnetopause shadowing (e.g. Ukhorskiy et al., 2006). Magnetopause shadowing  
 274 occurs when the ring current is strengthened and Earth's magnetic field strength is  
 275 increased outside of the ring current. If the ring current increases slowly enough (such  
 276 that  $J_3$  is conserved), a particle drift shell will move outward to conserve  $J_3$ . If the  
 277 particle's drift shell expands past the magnetopause, the particle will be lost to the  
 278 solar wind.

279 **Make sure I understand ULF waves and radial diffusion right** Another particle  
 280 loss (and acceleration) mechanism is driven by ultra low frequency (ULF) waves and  
 281 is called radial diffusion. Radial diffusion is the transport of particles from high  
 282 to low phase space density,  $f$ . If the transport is radially inward, particles will  
 283 appear to be accelerated. On the other hand, radially outward radial diffusion can  
 284 transport particles through the magnetopause where they will be lost to the solar  
 285 wind. Reeves et al. (2013) investigated the driver of particle acceleration during the

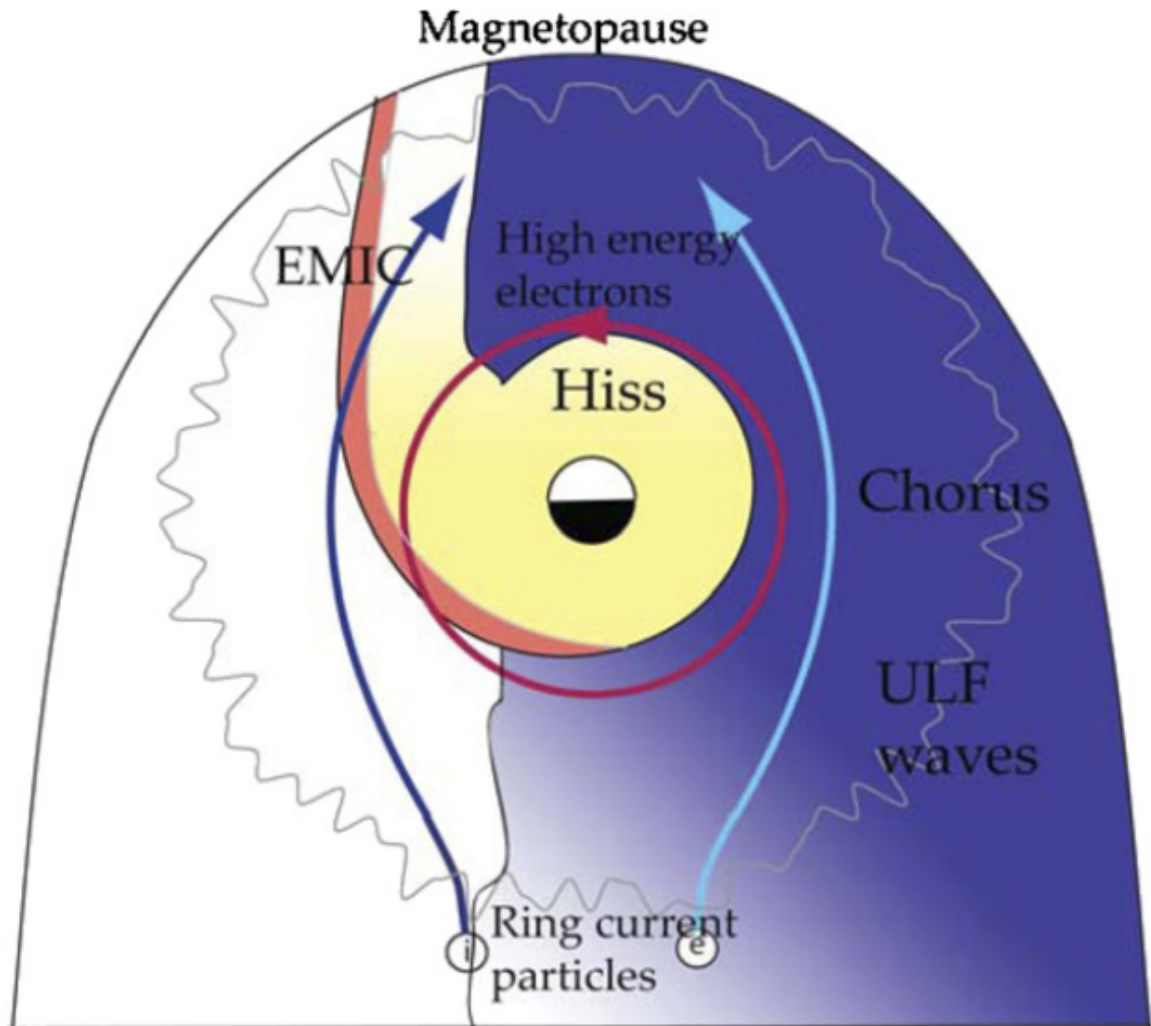


Figure 1.11: Various wave modes in the magnetosphere. Ultra low frequency waves occur through the magnetosphere. Chorus waves are typically observed in the 0-12 midnight-dawn region. EMIC waves are typically observed in the dusk MLT sector. Hiss waves are observed inside the plasmasphere. Figure from Millan and Thorne (2007).

286 October 2012 storm and observationally found that inward radial diffusion was not  
 287 dominant, rather local acceleration via wave-resonance heating appeared to be the  
 288 dominant acceleration mechanism.

289 The loss mechanism central to this dissertation is pitch angle and energy  
 290 scattering of electrons by waves. Some of the waves that scatter electrons in energy  
 291 and pitch angle in the inner magnetosphere are: plasmaspheric hiss (e.g. Breneman  
 292 et al., 2015; O'Brien et al., 2014), EMIC waves (e.g. Capannolo et al., 2019; Hendry  
 293 et al., 2017), and chorus waves (e.g. Breneman et al., 2017; Kasahara et al., 2018;  
 294 Ozaki et al., 2019). These wave-particle interactions occur when the resonance  
 295 condition in Eq. 1.22 is satisfied at which point the particle's energy and  $\alpha$  is modified  
 296 by the wave. More details regarding the theory of pitch angle and energy diffusion  
 297 is given in Chapter ???. If the wave changes  $\alpha$  towards 0 such that  $\alpha < \alpha_{LC}$ , the  
 298 particle's mirror point lowers to less than 100 km altitude where the particle can be  
 299 lost due collisions with air. One manifestation of pitch angle scattering of particles  
 300 into the loss cone are microbursts: a sub-second durtaison impulse of electrons.

301

### Microbursts

302 Microbursts were first found in high altitude balloon measurements of bremsstrahlung  
 303 X-rays emitted by microburst electrons impacting the atmosphere by Anderson  
 304 and Milton (1964). In the following years, numerous balloon flights expanded our  
 305 knowledge of non-relativistic microbursts (relativistic microbursts have not yet been  
 306 observed by high altitude balloons) by quantifying the microburst spatial extent,  
 307 temporal width, occurrence frequency, extent in L and MLT, and their source (a  
 308 local plasma instability vs. a propagating disturbance in the magnetosphere) (e.g.  
 309 Barcus et al., 1966; Brown et al., 1965; Parks, 1967; Trefall et al., 1966). Since then,  
 310 non-relativistic and relativistic ( $> 500$  keV) microbursts electrons have been directly

311 observed in LEO with spacecraft including the Solar Anomalous and Magnetospheric  
 312 Particle Explorer (SAMPEX) (e.g. Blake et al., 1996; Blum et al., 2015; Douma et al.,  
 313 2019, 2017; Greeley et al., 2019; Lorentzen et al., 2001a,b; Nakamura et al., 1995, 2000;  
 314 O'Brien et al., 2004, 2003), Montana State University's (MSU) Focused Investigation  
 315 of Relativistic Electron Bursts: Intensity, Range, and Dynamics II (FIREBIRD-II)  
 316 (Anderson et al., 2017; Breneman et al., 2017; Crew et al., 2016; Klumpar et al.,  
 317 2015; Spence et al., 2012), and Science Technologies Satellite (STSAT-I) (e.g. Lee  
 318 et al., 2012, 2005). An example microburst time series is shown in Fig. 1.12 and was  
 319 observed by the FIREBIRD-II CubeSats. The prominent features of the example  
 320 microbursts in Fig. 1.12 are their  $< 1$  second duration, half order of magnitude  
 321 increase in count rate above the falling background, and their approximately 200-800  
 322 keV energy extent.

323 Microbursts are observed on magnetic field footprints that are connected to the  
 324 outer radiation belt (approximately  $4 < L < 8$ ), and are predominately observed in  
 325 the 0-12 MLT sector with an elevated occurrence frequency during magnetospherically  
 326 disturbed times as shown in Fig. 1.13 (e.g. Douma et al., 2017). O'Brien et al. (2003)  
 327 used SAMPEX relativistic electron data and found that microbursts predominately  
 328 occur during the main phase of storms, with a heightened occurrence rate during the  
 329 recovery phase. Microburst occurrence rates also appear to be higher during high  
 330 solar wind velocity events e.g. from co-rotating interaction regions (Greeley et al.,  
 331 2019; O'Brien et al., 2003).

332 The impact of microbursts on atmospheric chemistry has been estimated to be  
 333 significant. Relativistic microburst electrons impacting the atmosphere are ionized at  
 334  $< 100$  km altitudes, with higher energy electrons penetrating closer to the surface.  
 335 The resulting chemical reaction of microburst electrons impacting the atmosphere  
 336 produces odd hydrogen HO<sub>x</sub> and odd nitrogen NO<sub>x</sub> molecules. These molecules are

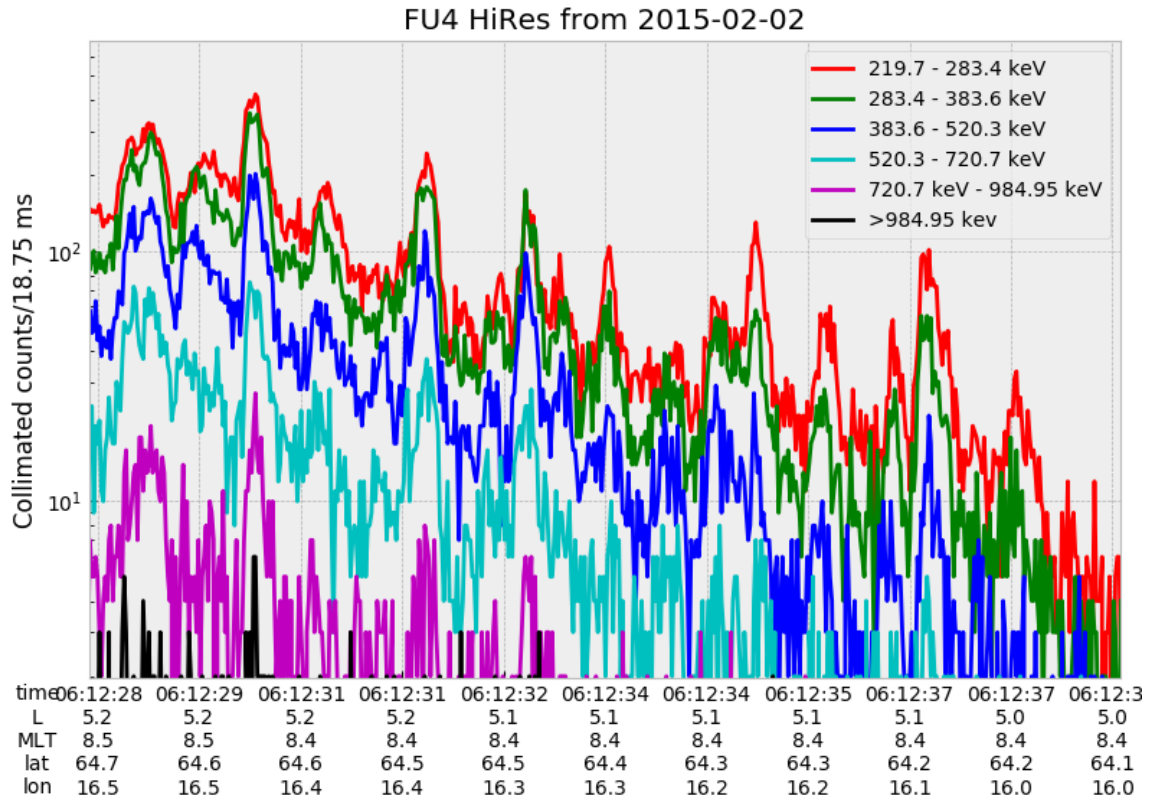


Figure 1.12: An example train of microbursts observed by FIREBIRD-II unit 4 on February 2nd, 2015. The colored curves show the differential energy channel count rates in six channels from  $\approx 200$  keV to greater than 1 MeV. The x-axis labels show auxiliary information such as time of observation and the spacecraft position in L, MLT, latitude and longitude coordinates.

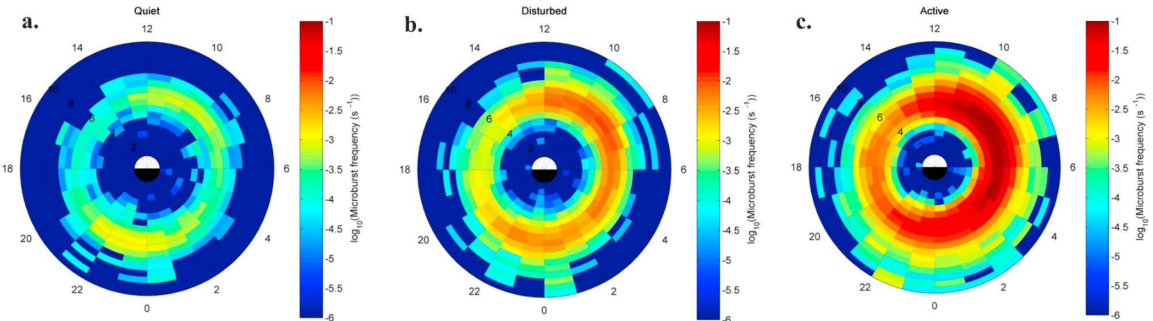


Figure 1.13: Relativistic ( $> 1\text{MeV}$ ) distribution of microburst occurrence rates as a function of  $L$  and MLT. The three panels show the microburst occurrence rate dependence on geomagnetic activity, parameterized by the auroral electrojet (AE) index for (a)  $\text{AE} < 100 \text{nT}$ , (b)  $100 < \text{AE} < 300 \text{nT}$  and (c)  $\text{AE} > 300 \text{nT}$ . Figure from Douma et al. (2017).

337 partially responsible for destroying ozone ( $\text{O}_3$ ). Seppälä et al. (2018) modeled a six  
 338 hour relativistic microburst storm and found that the mesospheric ozone was reduced  
 339 by 7 – 12% in the summer months and 12 – 20% in the winter months.

340 Furthermore, microbursts have also been estimated to have a significant impact  
 341 on the outer radiation belt electrons. Radiation belt electron loss due to microbursts  
 342 has been estimated to be on the order of a day (Breneman et al., 2017; Douma  
 343 et al., 2019; Lorentzen et al., 2001b; O’Brien et al., 2004; Thorne et al., 2005).

344 The wave-particle interactions responsible for generating microbursts are also  
 345 believed to accelerate electrons in the radiation belts. As mentioned earlier, when  
 346 an electron is in resonance with a wave, energy is exchanged with the wave and  
 347 the electron is either accelerated or decelerated. The signature of wave-particle  
 348 acceleration been observed for radiation belt electrons (e.g. Horne et al., 2005;  
 349 Meredith et al., 2002; Reeves et al., 2013). O’Brien et al. (2003) presented evidence  
 350 that enhancements in chorus waves, microbursts, and radiation belt electrons are  
 351 related. O’Brien et al. (2003) proposed an explanation where microburst precipitation  
 352 is a side effect of electron acceleration due to chorus waves. The widely used

353 theoretical framework to model interactions between electrons and chorus waves is  
 354 quasi-linear diffusion (e.g. Horne et al., 2005; Meredith et al., 2002; Summers, 2005;  
 355 Summers et al., 1998; Thorne et al., 2005; Walker, 1993) which is derived in Chapter  
 356 ???. Qualitatively, when a particle is resonant with a wave it can be transported in  
 357 pitch angle towards the loss cone and lose energy to the wave. In contrast, if the  
 358 particle is transported away from the loss cone, it gains energy from the wave.

359 The range of observed microburst energies range from a few tens of keV (e.g.  
 360 Datta et al., 1997; Parks, 1967) to greater than 1 MeV (e.g. Blake et al., 1996; Greeley  
 361 et al., 2019). The microburst electron flux ( $J$ ) falls off in energy, and the microburst  
 362 energy spectra is typically well fit to a decaying exponential

$$J(E) = J_0 e^{-E/E_0} \quad (1.23)$$

363 where  $J_0$  is the flux at 0 keV (unphysical free parameter) and  $E_0$  quantifies the  
 364 efficiency of the scattering mechanism in energy (.e.g Datta et al., 1997; Lee et al.,  
 365 2005; Parks, 1967). A small  $E_0$  suggests that mostly low energy particles are scattered  
 366 and a high  $E_0$  suggests that the scattering mechanism scatters low and high energy  
 367 electrons. Reality is a bit more messy and a high  $E_0$  may be a signature of a scattering  
 368 mechanism preferential to high energy electrons, but is hidden by the convolution of  
 369 the source particles available to be scattered (typically with a falling energy spectrum)  
 370 and the energy-dependent scattering efficiency.

371 The short duration of microbursts observed by a single LEO satellite has an  
 372 ambiguity when interpreting what is exactly a microburst. The two possible realities  
 373 are: a microburst is very small and spatially stationary so that the LEO spacecraft  
 374 passes through it in less than a second. Alternatively, microbursts are spatially large  
 375 with a short duration such that the microburst passes by the spacecraft in a fraction

376 of a second. There are a few ways to distinguish between the two possible realities,  
 377 and each one has a unique set of advantages.

378 A high altitude balloon provides essentially a stationary view of the precipitating  
 379 particles under the radiation belt footprints so a short-lived, temporal microburst can  
 380 be unambiguously identified. Spatial structures, on the other hand, are difficult to  
 381 identify because a balloon is essentially still on drift timescales.

382 Multi-spacecraft missions are an alternate solution which can determine if a  
 383 microburst-like feature is spatial or temporal. As will be shown in this dissertation,  
 384 if a microburst is observed simultaneously by two spacecraft then it is temporal and  
 385 has a size greater than the spacecraft separation. On the contrary, if two spacecraft  
 386 observe a microburst-like feature at different times, but at the same location, then  
 387 the feature is spatial and may be a curtain (Blake and O'Brien, 2016). Both balloon  
 388 and multi-spacecraft observational methods have a unique set of strengths, and this  
 389 dissertation takes the multi-spacecraft approach to identify and study microbursts.

390 Scope of Reserach

391 This dissertation furthers our understanding of the microburst scattering  
 392 mechanism by observing the scattering directly, and measuring the microburst sizes  
 393 and comparing them to the size of waves near the magnetic equator where those  
 394 electrons could have been scattered. Chapter ?? describes a microburst scattering  
 395 event observed by NASA's Van Allen Probes which was studied in the theoretic  
 396 framework of pitch angle and energy diffusion. The following two chapters will then  
 397 study the size of microbursts. Chapter ?? describes a bouncing packet microburst  
 398 observation made by MSU's FIREBIRD-II mission where the microburst's lower  
 399 bound longitudinal and latitudinal sizes were estimated. Then Chapter ?? expands  
 400 the case study from Ch. ?? to a statistical study of microburst sizes using The

401 Aerospace Corporation's AeroCube-6 (AC6) CubeSats. In this study, a Monte Carlo  
402 and analytic microburst size models were developed to account for the compounding  
403 effects of random microburst sizes and locations. Lastly, Chapter ?? will summarize  
404 the dissertation work and make concluding remarks regarding outstanding questions  
405 in microburst physics.

## Bibliography

- 407 Anderson, B., Shekhar, S., Millan, R., Crew, A., Spence, H., Klumpar, D., Blake, J.,  
 408 O'Brien, T., and Turner, D. (2017). Spatial scale and duration of one microburst  
 409 region on 13 August 2015. *Journal of Geophysical Research: Space Physics*.
- 410 Anderson, K. A. and Milton, D. W. (1964). Balloon observations of X rays in the  
 411 auroral zone: 3. High time resolution studies. *Journal of Geophysical Research*,  
 412 69(21):4457–4479.
- 413 Barcus, J., Brown, R., and Rosenberg, T. (1966). Spatial and temporal character of  
 414 fast variations in auroral-zone x rays. *Journal of Geophysical Research*, 71(1):125–  
 415 141.
- 416 Baumjohann, W. and Treumann, R. A. (1997). *Basic space plasma physics*. World  
 417 Scientific.
- 418 Blake, J.,Looper, M., Baker, D., Nakamura, R., Klecker, B., and Hovestadt, D.  
 419 (1996). New high temporal and spatial resolution measurements by sampex of the  
 420 precipitation of relativistic electrons. *Advances in Space Research*, 18(8):171 – 186.
- 421 Blake, J. B. and O'Brien, T. P. (2016). Observations of small-scale latitudinal  
 422 structure in energetic electron precipitation. *Journal of Geophysical Research: Space  
 423 Physics*, 121(4):3031–3035. 2015JA021815.
- 424 Blum, L., Li, X., and Denton, M. (2015). Rapid MeV electron precipitation as  
 425 observed by SAMPEX/HILT during high-speed stream-driven storms. *Journal of  
 426 Geophysical Research: Space Physics*, 120(5):3783–3794. 2014JA020633.
- 427 Breneman, A., Crew, A., Sample, J., Klumpar, D., Johnson, A., Agapitov, O.,  
 428 Shumko, M., Turner, D., Santolik, O., Wygant, J., et al. (2017). Observations  
 429 directly linking relativistic electron microbursts to whistler mode chorus: Van allen  
 430 probes and FIREBIRD II. *Geophysical Research Letters*.
- 431 Breneman, A. W., Halford, A., Millan, R., McCarthy, M., Fennell, J., Sample, J.,  
 432 Woodger, L., Hospodarsky, G., Wygant, J. R., Cattell, C. A., et al. (2015). Global-  
 433 scale coherence modulation of radiation-belt electron loss from plasmaspheric hiss.  
 434 *Nature*, 523(7559):193.
- 435 Brown, R., Barcus, J., and Parsons, N. (1965). Balloon observations of auroral zone  
 436 x rays in conjugate regions. 2. microbursts and pulsations. *Journal of Geophysical  
 437 Research (U.S.)*.
- 438 Capannolo, L., Li, W., Ma, Q., Shen, X.-C., Zhang, X.-J., Redmon, R., Rodriguez,  
 439 J., Engebretson, M., Kletzing, C., Kurth, W., et al. (2019). Energetic electron  
 440 precipitation: multi-event analysis of its spatial extent during emic wave activity.  
 441 *Journal of Geophysical Research: Space Physics*.

- 442 Claudepierre, S., O'Brien, T.,Looper, M., Blake, J., Fennell, J., Roeder, J.,  
 443 Clemmons, J., Mazur, J., Turner, D., Reeves, G., et al. (2019). A revised look  
 444 at relativistic electrons in the earth's inner radiation zone and slot region. *Journal*  
 445 *of Geophysical Research: Space Physics*, 124(2):934–951.
- 446 Crew, A. B., Spence, H. E., Blake, J. B., Klumpar, D. M., Larsen, B. A., O'Brien,  
 447 T. P., Driscoll, S., Handley, M., Legere, J., Longworth, S., Mashburn, K.,  
 448 Mosleh, E., Ryhajlo, N., Smith, S., Springer, L., and Widholm, M. (2016). First  
 449 multipoint in situ observations of electron microbursts: Initial results from the  
 450 NSF FIREBIRD II mission. *Journal of Geophysical Research: Space Physics*,  
 451 121(6):5272–5283. 2016JA022485.
- 452 Datta, S., Skoug, R., McCarthy, M., and Parks, G. (1997). Modeling of microburst  
 453 electron precipitation using pitch angle diffusion theory. *Journal of Geophysical*  
 454 *Research: Space Physics*, 102(A8):17325–17333.
- 455 Douma, E., Rodger, C., Blum, L., O'Brien, T., Clilverd, M., and Blake, J. (2019).  
 456 Characteristics of relativistic microburst intensity from sampex observations.  
 457 *Journal of Geophysical Research: Space Physics*.
- 458 Douma, E., Rodger, C. J., Blum, L. W., and Clilverd, M. A. (2017). Occurrence  
 459 characteristics of relativistic electron microbursts from SAMPEX observations.  
 460 *Journal of Geophysical Research: Space Physics*, 122(8):8096–8107. 2017JA024067.
- 461 Eastwood, J., Hietala, H., Toth, G., Phan, T., and Fujimoto, M. (2015). What  
 462 controls the structure and dynamics of earths magnetosphere? *Space Science*  
 463 *Reviews*, 188(1-4):251–286.
- 464 Greeley, A., Kanekal, S., Baker, D., Klecker, B., and Schiller, Q. (2019). Quantifying  
 465 the contribution of microbursts to global electron loss in the radiation belts. *Journal*  
 466 *of Geophysical Research: Space Physics*.
- 467 Hendry, A. T., Rodger, C. J., and Clilverd, M. A. (2017). Evidence of sub-mev  
 468 emic-driven electron precipitation. *Geophysical Research Letters*, 44(3):1210–1218.
- 469 Horne, R., Glauert, S., Meredith, N., Boscher, D., Maget, V., Heynderickx, D., and  
 470 Pitchford, D. (2013). Space weather impacts on satellites and forecasting the earth's  
 471 electron radiation belts with spacecast. *Space Weather*, 11(4):169–186.
- 472 Horne, R. B., Thorne, R. M., Shprits, Y. Y., Meredith, N. P., Glauert, S. A., Smith,  
 473 A. J., Kanekal, S. G., Baker, D. N., Engebretson, M. J., Posch, J. L., et al.  
 474 (2005). Wave acceleration of electrons in the van allen radiation belts. *Nature*,  
 475 437(7056):227.
- 476 Kasahara, S., Miyoshi, Y., Yokota, S., Mitani, T., Kasahara, Y., Matsuda, S.,  
 477 Kumamoto, A., Matsuoka, A., Kazama, Y., Frey, H., et al. (2018). Pulsating  
 478 aurora from electron scattering by chorus waves. *Nature*, 554(7692):337.

- 479 Klumpar, D., Springer, L., Mosleh, E., Mashburn, K., Berardinelli, S., Gunderson,  
 480 A., Handly, M., Ryhajlo, N., Spence, H., Smith, S., Legere, J., Widholm, M.,  
 481 Longworth, S., Crew, A., Larsen, B., Blake, J., and Walmsley, N. (2015). Flight  
 482 system technologies enabling the twin-cubesat firebird-ii scientific mission.
- 483 Lee, J. J., Parks, G. K., Lee, E., Tsurutani, B. T., Hwang, J., Cho, K. S., Kim, K.-H.,  
 484 Park, Y. D., Min, K. W., and McCarthy, M. P. (2012). Anisotropic pitch angle  
 485 distribution of 100 keV microburst electrons in the loss cone: measurements from  
 486 STSAT-1. *Annales Geophysicae*, 30(11):1567–1573.
- 487 Lee, J.-J., Parks, G. K., Min, K. W., Kim, H. J., Park, J., Hwang, J., McCarthy,  
 488 M. P., Lee, E., Ryu, K. S., Lim, J. T., Sim, E. S., Lee, H. W., Kang, K. I., and  
 489 Park, H. Y. (2005). Energy spectra of 170–360 keV electron microbursts measured  
 490 by the korean STSAT-1. *Geophysical Research Letters*, 32(13). L13106.
- 491 Li, X., Selesnick, R., Schiller, Q., Zhang, K., Zhao, H., Baker, D. N., and Temerin,  
 492 M. A. (2017). Measurement of electrons from albedo neutron decay and neutron  
 493 density in near-earth space. *Nature*, 552(7685):382.
- 494 Lorentzen, K. R., Blake, J. B., Inan, U. S., and Bortnik, J. (2001a). Observations  
 495 of relativistic electron microbursts in association with VLF chorus. *Journal of  
 496 Geophysical Research: Space Physics*, 106(A4):6017–6027.
- 497 Lorentzen, K. R., Looper, M. D., and Blake, J. B. (2001b). Relativistic electron  
 498 microbursts during the GEM storms. *Geophysical Research Letters*, 28(13):2573–  
 499 2576.
- 500 Lyons, L. R. and Thorne, R. M. (1973). Equilibrium structure of radiation belt  
 501 electrons. *Journal of Geophysical Research*, 78(13):2142–2149.
- 502 Meredith, N., Horne, R., Summers, D., Thorne, R., Iles, R., Heynderickx, D., and  
 503 Anderson, R. (2002). Evidence for acceleration of outer zone electrons to relativistic  
 504 energies by whistler mode chorus. In *Annales Geophysicae*, volume 20, pages 967–  
 505 979.
- 506 Millan, R. and Thorne, R. (2007). Review of radiation belt relativistic electron losses.  
 507 *Journal of Atmospheric and Solar-Terrestrial Physics*, 69(3):362 – 377.
- 508 Nakamura, R., Baker, D. N., Blake, J. B., Kanekal, S., Klecker, B., and Hovestadt,  
 509 D. (1995). Relativistic electron precipitation enhancements near the outer edge of  
 510 the radiation belt. *Geophysical Research Letters*, 22(9):1129–1132.
- 511 Nakamura, R., Isowa, M., Kamide, Y., Baker, D., Blake, J., and Looper, M. (2000).  
 512 Observations of relativistic electron microbursts in association with VLF chorus.  
 513 *J. Geophys. Res.*, 105:15875–15885.

- 514 O'Brien, T., Claudepierre, S., Blake, J., Fennell, J. F., Clemons, J., Roeder, J.,  
 515 Spence, H. E., Reeves, G., and Baker, D. (2014). An empirically observed pitch-  
 516 angle diffusion eigenmode in the earth's electron belt near  $l^* = 5.0$ . *Geophysical*  
 517 *Research Letters*, 41(2):251–258.
- 518 O'Brien, T., Claudepierre, S., Guild, T., Fennell, J., Turner, D., Blake, J., Clemons,  
 519 J., and Roeder, J. (2016). Inner zone and slot electron radial diffusion revisited.  
 520 *Geophysical Research Letters*, 43(14):7301–7310.
- 521 O'Brien, T. and Moldwin, M. (2003). Empirical plasmapause models from magnetic  
 522 indices. *Geophysical Research Letters*, 30(4).
- 523 O'Brien, T. P.,Looper, M. D., and Blake, J. B. (2004). Quantification of relativistic  
 524 electron microburst losses during the GEM storms. *Geophysical Research Letters*,  
 525 31(4). L04802.
- 526 O'Brien, T. P., Lorentzen, K. R., Mann, I. R., Meredith, N. P., Blake, J. B., Fennell,  
 527 J. F.,Looper, M. D., Milling, D. K., and Anderson, R. R. (2003). Energization of  
 528 relativistic electrons in the presence of ULF power and MeV microbursts: Evidence  
 529 for dual ULF and VLF acceleration. *Journal of Geophysical Research: Space*  
 530 *Physics*, 108(A8).
- 531 Ozaki, M., Miyoshi, Y., Shiokawa, K., Hosokawa, K., Oyama, S.-i., Kataoka, R.,  
 532 Ebihara, Y., Ogawa, Y., Kasahara, Y., Yagitani, S., et al. (2019). Visualization of  
 533 rapid electron precipitation via chorus element wave–particle interactions. *Nature*  
 534 *communications*, 10(1):257.
- 535 Parks, G. K. (1967). Spatial characteristics of auroral-zone X-ray microbursts. *Journal*  
 536 *of Geophysical Research*, 72(1):215–226.
- 537 Reeves, G., Spence, H. E., Henderson, M., Morley, S., Friedel, R., Funsten, H., Baker,  
 538 D., Kanekal, S., Blake, J., Fennell, J., et al. (2013). Electron acceleration in the  
 539 heart of the van allen radiation belts. *Science*, 341(6149):991–994.
- 540 Reeves, G. D., McAdams, K. L., Friedel, R. H. W., and O'Brien, T. P. (2003). Ac-  
 541 celeration and loss of relativistic electrons during geomagnetic storms. *Geophysical*  
 542 *Research Letters*, 30(10):n/a–n/a. 1529.
- 543 Schulz, M. and Lanzerotti, L. J. (1974). *Particle Diffusion in the Radiation Belts*.  
 544 Springer.
- 545 Seppälä, A., Douma, E., Rodger, C., Verronen, P., Clilverd, M. A., and Bortnik, J.  
 546 (2018). Relativistic electron microburst events: Modeling the atmospheric impact.  
 547 *Geophysical Research Letters*, 45(2):1141–1147.

- 548 Spence, H. E., Blake, J. B., Crew, A. B., Driscoll, S., Klumpar, D. M., Larsen,  
 549 B. A., Legere, J., Longworth, S., Mosleh, E., O'Brien, T. P., Smith, S., Springer,  
 550 L., and Widholm, M. (2012). Focusing on size and energy dependence of electron  
 551 microbursts from the van allen radiation belts. *Space Weather*, 10(11).
- 552 Summers, D. (2005). Quasi-linear diffusion coefficients for field-aligned electro-  
 553 magnetic waves with applications to the magnetosphere. *Journal of Geophysical  
 554 Research: Space Physics*, 110(A8):n/a–n/a. A08213.
- 555 Summers, D., Thorne, R. M., and Xiao, F. (1998). Relativistic theory of wave-particle  
 556 resonant diffusion with application to electron acceleration in the magnetosphere.  
 557 *Journal of Geophysical Research: Space Physics*, 103(A9):20487–20500.
- 558 Thorne, R. M., O'Brien, T. P., Shprits, Y. Y., Summers, D., and Horne, R. B. (2005).  
 559 Timescale for MeV electron microburst loss during geomagnetic storms. *Journal  
 560 of Geophysical Research: Space Physics*, 110(A9). A09202.
- 561 Trefall, H., Bjordal, J., Ullaland, S., and Stadsnes, J. (1966). On the extension of  
 562 auroral-zone x-ray microbursts. *Journal of Atmospheric and Terrestrial Physics*,  
 563 28(2):225–233.
- 564 Tsurutani, B. T. and Lakhina, G. S. (1997). Some basic concepts of wave-particle  
 565 interactions in collisionless plasmas. *Reviews of Geophysics*, 35(4):491–501.
- 566 Ukhorskiy, A. Y., Anderson, B. J., Brandt, P. C., and Tsyganenko, N. A. (2006).  
 567 Storm time evolution of the outer radiation belt: Transport and losses. *Journal of  
 568 Geophysical Research: Space Physics*, 111(A11):n/a–n/a. A11S03.
- 569 Van Allen, J. A. (1959). The geomagnetically trapped corpuscular radiation. *Journal  
 570 of Geophysical Research*, 64(11):1683–1689.
- 571 Vernov, S. and Chudakov, A. (1960). Investigation of radiation in outer space. In  
 572 *International Cosmic Ray Conference*, volume 3, page 19.
- 573 Walker, A. D. M. (1993). *Plasma waves in the magnetosphere*, volume 24. Springer  
 574 Science & Business Media.